A&A 673, A162 (2023)
https://doi.org/10.1051/0004-6361/202345869


Astronomy & Astrophysics

# Prediction of gamma-ray emission from Cygnus X-1, SS 433, and GRS 1915+105 after absorption

Th. V. Papavasileiou[1], O. T. Kosmas[2], and I. Sinatkas[1]

[1] Department of Informatics, University of Western Macedonia, Fourka Area, 52100 Kastoria, Greece
e-mail: th.papavasileiou@uowm.gr
[2] Department of MACE, University of Manchester, Sackville Street, George Begg Building, M1 3BB Manchester, UK

Received 9 January 2023 / Accepted 4 April 2023

**ABSTRACT**

*Context.* Stellar black hole X-ray binary stars (BHXRBs) are among the most luminous and powerful systems located in our Milky Way and in other galaxies of the Universe. Their jets are prominent sources of particles (e.g., neutrinos) and radiation emissions in energy ranges detectable by terrestrial and space telescopes, even from galaxies deep in the space. A significant factor, however, would be the photon absorption effect that occur due to scattering on the lower end of the energy radiation of the system's surroundings.
*Aims.* We aim to study in detail and extract predictions for the emitted gamma-ray intensities and integral fluxes of the jets emanating from BHXRB systems Cygnus X-1, GRS 1915+105, and SS 433. Toward this end, we also investigate the severe effects of gamma-ray absorption that eradicate part of the produced intensity spectra. Furthermore, we explore the jet regions that are most likely to emit unabsorbed gamma-rays capable of reaching detectors on Earth. Our goal is to calculate the integral fluxes before and after absorption for the abovementioned systems and compare the results with the very-high-energy gamma-ray observations of sensitive telescopes such as the MAGIC, H.E.S.S., *Fermi*-LAT, and so on.
*Methods.* The implemented gamma-ray emission mechanisms initiate from the $p-p$ scattering process inside the hadron-dominated jets following the well-known shock-wave particle acceleration. In addition, we estimate the optical depths of three absorption processes between gamma-ray photons and (i) accretion disk X-ray emission, (ii) black hole corona photons, and (iii) donor star thermal emission. We also examine the dependence of the absorption optical depths on various parameters, such as the disk's temperature, coronal radius and, donor star luminosity.
*Results.* We find that disk absorption is dominant for distances of $z < 10^{10}$ cm from the black hole, while the donor star absorption dominates for $10^{10} < z < 10^{12}$ cm. Beyond that jet point, the absorption effects become significantly weaker. Cygnus X-1 presents the highest gamma-ray integral flux across the jet length, while GRS 1915+105 emits the least due to its weakly collimated jets. The jets of SS 433 emit gamma-rays only for $z > 10^{10}$ cm due to severe disk absorption fueled by the system's super-Eddington accretion limit.

**Key words.** acceleration of particles – accretion, accretion disks – stars: black holes – X-rays: binaries – opacity – radiation mechanisms: non-thermal

## 1. Introduction

In recent decades, the investigation of particle and radiation emissions from black hole binary stars has attracted much attention among researchers dealing with compact systems located inside galaxies – specifically, in our Galaxy and neighboring ones such as the Large Magellanic Cloud, the Messier, and others. Their magnetohydrodynamical plasma outflows (jets), emitted from the central region of the compact objects, are often considered as leptonic and hadronic matter that is accelerated and collimated by the system's magnetic field. Geometrically, these jets may, to a good approximation, be described as conic (Romero et al. 2017) with the half-opening angle ($\xi$) dependent on the magnetic field intensity, B.

Concerning the detection of gamma-rays from the SS 433 black hole microquasar, up to now, several attempts have been made with many Cherenkov telescopes (HEGRA, MAGIC, INTEGRAL, etc.). In a recent effort by MAGIC, there was no clear signal traced for very-high-energy (VHE) gamma-ray emission (Ahnen et al. 2018). However, upper photon flux limits such as $\Phi_\gamma \leq 10^{-12}\,\mathrm{ph\,cm^{-2}\,s^{-1}}$, were established for $E_\gamma \sim 10^2$ GeV by the HEGRA and MAGIC telescopes (Aharonian et al. 2005; Saito et al. 2009; Ahnen et al. 2018). On the other hand, theoretical predictions for this system suggest gamma-ray production at distances $z \geq 10^{13}$ cm (Bordas et al. 2010). In addition, emission in the TeV regime was observed from SS 433 by HAWC (Abeysekara et al. 2018), although they likely stem from the jet interaction region with the interstellar medium. The suggested mechanisms are charged-leptons acceleration (e.g., synchrotron radiation, inverse Compton scattering) in addition to hadron (e.g., $\pi_0$, $\eta$) decays.

For the Cygnus X-1 system, there have been multiple recent attempts carried out to observe high-energy gamma-ray emissions. In particular, the *Fermi*-LAT detected radiation in the $E_\gamma \approx 0.06$–$20$ GeV range, with luminosity $L = 5.5 \times 10^{33}\,\mathrm{erg\,s^{-1}}$ associated with the system's relativistic jets (Zanin et al. 2016) during their hard X-ray period. This spectrum fits a power-law distribution ($\propto E_\gamma^{-\alpha}$), with $\alpha \approx 2.3$. Furthermore, indications suggest that the emission region is constrained to distances $z = 10^{11}$–$10^{13}$ cm from the black hole object (Zanin et al. 2016). Moreover, other emissions reported are likely associated with the three flaring events that occurred between 2009 and 2010 than with the system's hard state. Additionally, during another flaring activity in 2006, the MAGIC telescope detected

gamma-ray emission from Cygnus X-1 in the high-energy regime ($E_\gamma \geq 10^2$ GeV; Albert et al. 2007) that confirms, for the first time, an unbroken power-law spectrum from an X-ray binary system (i.e., XRB). However, this was not associated with a steady gamma-ray emission event. Recently, there was another attempt towards observing VHE gamma-rays ($E_\gamma > 200$ GeV) by the MAGIC Collaboration (Ahnen et al. 2017) that was proven fruitless and led to the establishment of an integral flux upper limit of $\Phi_\gamma < 2.6 \times 10^{-12}$ ph cm$^{-2}$ s$^{-1}$.

Regarding the weakly collimated jets of the GRS 1915+105 system, significant VHE gamma-ray attempts at observation have failed. Thus, through the measured integral fluxes, only upper limits were established as $\Phi_\gamma < 2.3 \times 10^{-8}$ ph cm$^{-2}$ s$^{-1}$ for $E_\gamma = 0.1-10$ GeV (Bodaghee et al. 2013, *Fermi*-LAT), $\Phi_\gamma < 0.61 \times 10^{-12}$ ph cm$^{-2}$ s$^{-1}$ for $E_\gamma > 410$ GeV (Szostek et al. 2009; Acero et al. 2009, H.E.S.S.), $\Phi_\gamma < 7.3 \times 10^{-13}$ ph cm$^{-2}$ s$^{-1}$ for $E_\gamma > 560$ GeV (Abdalla et al. 2018, H.E.S.S.), and $\Phi_\gamma < 1.1 \times 10^{-13}$ ph cm$^{-2}$ s$^{-1}$ for $E_\gamma > 1101$ GeV (Schüssler et al. 2015, H.E.S.S.). In brief, we can conclude that there is a lack of persistent high-energy gamma-ray observations for the GRS 1915+105 binary system.

In the present work, we attempt to obtain predictions for integral gamma-ray fluxes emitted from the jets of the aforementioned black hole X-ray binary systems, Cygnus X-1, GRS 1915+105, and SS 433, by implementing the recently redefined parameters for these systems. With this intention, we employed a hadronic model that assumes a cold-matter-dominated jet, similarly to the work of Bosch-Ramon et al. (2006) and Reynoso & Romero (2009). We used a multi-zone approach since our focus is on multiple non-overlapping acceleration zones over the extended length of the jet (also discussed in our previous works Papavasileiou et al. 2021a, 2022). This model is based on the decay of neutral pions ($\pi_0$) produced from $p-p$ scatterings of cold jet protons with accelerated (relativistic) ones. As is well known, the hadron acceleration takes place in well-defined jet regions at various distances from the black hole.

In our investigation, we also consider the damaging effect of ambient photon fields emitted by the system's environment. That includes the overheated accretion disk, the black hole's corona and the system's donor star. Towards this purpose, we adopt a geometrical analysis similar to that of Cerutti et al. (2011), and Böttcher & Dermer (2005). We note that in our previous works (Papavasileiou et al. 2021a, 2022), we calculated gamma-ray and neutrino intensities for the extragalactic BHXRB LMC X-1 that also emerge through the $p-p$ collision channels, while considering the $p-\gamma$ interactions as well.

Our goal is to explain the lack of VHE observations from the three widely studied XRBs and the significance of the various absorption mechanisms. For that purpose, we prioritized the geometrical aspects of those components and consider several intrinsic parameters that are neglected in many model studies, especially in the case of the accretion disk, which constitutes the most crucial source of photon absorption.

The rest of the paper is organized as follows. Initially, in Sect. 2, we present the employed hadronic model for gamma-ray production. In Sect. 3, we discuss three different kinds of absorption from the accretion disk, corona, and the donor star, along with their dependence on the distance from the black hole and including other sensitive parameters. In Sect. 4, we calculate the expected gamma-ray intensities before and after absorption, along with the respective integral fluxes for the three black hole X-ray binary systems: Cygnus X-1, SS 433, and GRS 1915+105. Finally, in Sect. 5, we summarize the main conclusions extracted from the present investigation.

## 2. Particle acceleration and gamma-ray production

### 2.1. Proton acceleration and cooling

The hadronic jets are characterized by the hadron-to-lepton ratio $\alpha_k = L_p/L_e$, where $L_p$ ($L_e$) stands for the proton (electron) kinetic luminosity. For high values of this ratio, the protons of the jet essentially carry most of its kinetic luminosity. A portion of the hadronic jet content (defined by a parameter $q_{rel}$) accelerates through shock-waves to relativistic energies due to the known second-order *Fermi* mechanism in a zone that begins from $z_0$, measured from the compact object and is extended up to $z_{max}$ (one-zone approximation; Khangulyan et al. 2007). The relativistic protons collide with the cold (non-accelerated) ones inside the jet resulting in a multi-species (pions, muons, neutrinos, gamma-rays, etc.) reaction chain.

In the model employed (Reynoso et al. 2008; Reynoso & Romero 2009; Reynoso & Carulli 2019), the jets are deemed conic along the ejection $z$-axis with a half-opening angle $\xi$ (Marshall et al. 2002), as illustrated in Fig. 1. The acceleration rate within the zone between $z_0$ and $z_{max}$ is given by (Gallant & Achterberg 1999):

$$t_{acc}^{-1} \simeq \frac{\eta c e B}{E}, \tag{1}$$

with $e$ being the electron/proton charge and $\eta$ the acceleration efficiency (see Table B.1; Begelman et al. 1990). The system's magnetic field $B$ is equal to $B = \sqrt{8\pi\rho_k(z)}$, where the parameter $\rho_k$ denotes the kinetic energy density of the jet (see reference Reynoso et al. 2008; Reynoso & Romero 2009; Smponias & Kosmas 2011, 2013; Kosmas & Smponias 2018). The resulting distribution in the jet's rest frame is given by $N'(E') \sim E'^{-2}$ [GeV$^{-1}$ cm$^{-3}$] (power-law). In the above model, about 10% of the system's Eddington luminosity is essentially transferred into the jets for acceleration and collimation, namely, $L_k \approx 0.1\, L_{Edd}$ (Körding et al. 2006).

Naturally, acceleration is not the only energy-altering mechanism affecting jet particles. Protons (and the other produced particles) lose energy due to collisions with the rest of the jet's content ($t_{pp}^{-1}$), synchrotron radiation emission ($t_{sync}^{-1}$), jet's (adiabatic) expansion towards the ejection axis ($t_{ad}^{-1}$), etc. The associated rate of each mechanism is given as follows:

$$t_{ad}^{-1} = \frac{2\upsilon_b}{3z}, \tag{2}$$

$$t_{pp}^{-1} = \frac{1}{2} n(z) c \sigma_{pp}^{inel}(E), \tag{3}$$

$$t_{sync}^{-1} = \frac{4}{3}\left(\frac{m_e}{m}\right)^3 \frac{\sigma_T B^2}{8\pi m_e c}\gamma, \tag{4}$$

where $\upsilon_b$ is the jet's bulk velocity, $\gamma = E/mc^2$ and $\sigma_T$, the well-known Thomson cross-section, as listed in Table B.1. The inelastic $p-p$ collision cross-section, $\sigma_{pp}^{inel}$, is provided in the Appendix B.1. It should be mentioned that, given the definition of $t_{pp}^{-1}$, the cold proton density $n(z)$ is expressed as:

$$n(z) = \frac{(1-q_{rel})L_k}{\Gamma_b m_p c^2 \pi r(z)^2 \upsilon_b}, \tag{5}$$

where $\Gamma_b$ represents the Lorentz factor corresponding to the jet's velocity. For a thorough discussion of the above mechanisms, the reader is referred, for instance, to Papavasileiou et al. (2021b), and references therein.

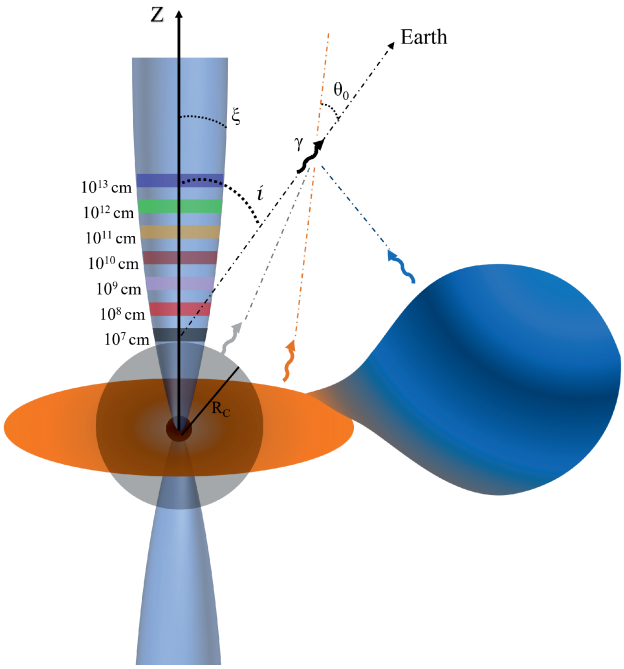


**Fig. 1.** Shematic approach of a black hole X-ray binary system.

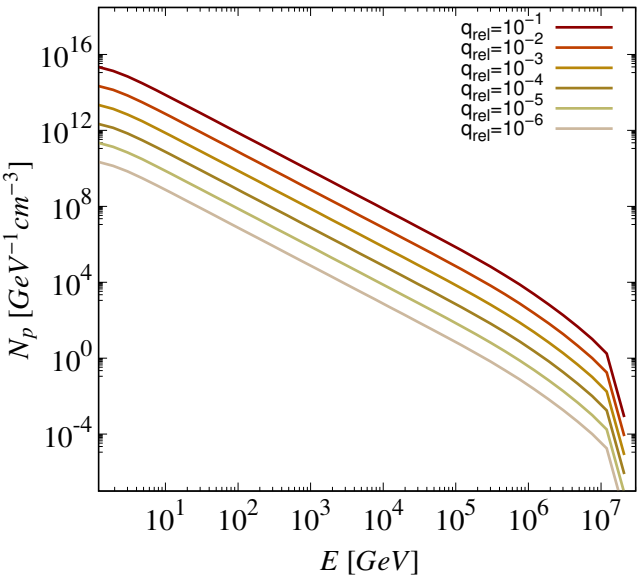


**Fig. 2.** Proton energy distribution for different values of the parameter $q_{\rm rel}$ assuming $z = 5\,R_{\rm Sch}/\tan\xi \approx 10^9$ cm for the binary system Cygnus X-1.

The proton's maximum energy $E_{\rm max}$ can be found by equating the energy-gain and energy-loss rates as

$$t_{\rm acc}^{-1}(E_{\rm max}) = t_{\rm loss}^{-1}(E_{\rm max}), \tag{6}$$

definition which is applied below (see Sect. 2.2).

### 2.2. Particle energy distributions

A power-law source function that satisfactorily describes the accelerated relativistic protons was proposed in previous works (Achterberg et al. 2001; Kirk et al. 2000) and expressed as:

$$Q(E', z) = Q_0 \left(\frac{z_0}{z}\right)^3 E'^{-2}, \tag{7}$$

where $z$ ($z_0 \le z \le z_{\rm max}$) denotes the distance from $z_0$ of a vertical on the $z$-axis level inside the emission (acceleration) region of the jet. The normalization constant $Q_0$ emerges through the proton total luminosity integration (see Appendix A.1). Furthermore, the transformation of Eq. (7) to the observer's reference frame is written as (Torres & Reimer 2011):

$$Q(E, z) = Q_0 \left(\frac{z_0}{z}\right)^3 \frac{\Gamma_b^{-1}\left(E - \beta_b \cos i \sqrt{E^2 - m^2c^4}\right)^{-2}}{\sqrt{\sin^2 i + \Gamma_b^2\left(\cos i - \frac{\beta_b E}{\sqrt{E^2 - m^2c^4}}\right)^2}}, \tag{8}$$

where $\Gamma_{\rm b}$ denotes the Lorentz factor that corresponds to the jet's bulk velocity, $\upsilon_{\rm b} = \beta_{\rm b} c$, and $i$ the angle between the jet-axis and line-of-sight direction (also known as the inclination of the system), as illustrated in Fig. 1.

By assuming steady-state jets, the proton energy distribution $N(E, z)$ is provided by the solution of the relevant transfer equation (Romero et al. 2003; Zhang et al. 2017):

$$\frac{\partial N(E,z) b(E,z)}{\partial E} + t^{-1} N(E,z) = Q(E,z). \tag{9}$$

The injection function $Q(E, z)$ is taken from Eq. (8) and represents the proton production rate (in GeV$^{-1}$ cm$^{-3}$ s$^{-1}$). The energy-loss rate due to the aforementioned cooling mechanisms of the particles (protons) is $b(E) = {\rm d}E/{\rm d}t = -Et_{\rm loss}^{-1}$. In addition, the particle reduction rate (due to their escape from the jet or decaying in the case of pions and muons) inside the jet is given by $t^{-1} = t_{\rm esc}^{-1} + t_{\rm dec}^{-1}$. For the escape rate, it holds that $t_{\rm esc}^{-1} \approx c/(z_{\rm max} - z)$. At this point, it is worth noting that the independence (from time) of particle distributions inside the jet in the assumed steady-state approximation of Eq. (9) is justified due to the time-scale of the astrophysical phenomena as well as the discussed mechanisms.

The general solution of Eq. (9) is written as

$$N(E, z) = \frac{1}{|\, b(E)\,|} \int_{\rm E}^{E_{\rm max}} Q(E', z) e^{-\tau(E,E')} {\rm d}E', \tag{10}$$

where

$$\tau(E, E') = \int_{\rm E}^{E'} \frac{{\rm d}E'' t^{-1}}{|\, b(E'')\,|}. \tag{11}$$

In Fig. 2, we illustrate the proton energy distributions $N(E, z)$ that correspond to six values of the free parameter $q_{\rm rel}$. We implemented the highest value in our results that constitutes an upper limit to gamma-ray production efficiency, but we also made a comparison with lower, more realistic $q_{\rm rel}$ values as well.

### 2.3. Gamma-ray emission

In general, gamma-ray photons are products of neutral pions ($\pi^0$) and eta-mesons ($\eta$) decay described by the reactions

$$\pi^0 \rightarrow \gamma + \gamma, \tag{12}$$

$$\eta \rightarrow \gamma + \gamma. \tag{13}$$

The decay of neutral pions (products of the inelastic $p-p$ collisions) composes the leading contributing process to the jet's gamma-ray emission. Recent simulations have shown that the respective gamma-ray spectra, as functions of the energy $E_\gamma = xE_{\rm p}$, are fitted by the expression such as that proposed in

Kelner et al. (2006)

$$F_\gamma(x, E_p) = B_\gamma \frac{\ln x}{x}\left(\frac{1-x^{\beta_\gamma}}{1+k_\gamma x^{\beta_\gamma}(1-x^{\beta_\gamma})}\right)^4 \times\left(\frac{1}{\ln x}-\frac{4\beta_\gamma x^{\beta_\gamma}}{1-x^{\beta_\gamma}}-\frac{4k_\gamma\beta_\gamma x^{\beta_\gamma}(1-2x^{\beta_\gamma})}{1+k_\gamma x^{\beta_\gamma}(1-x^{\beta_\gamma})}\right), \quad (14)$$

where the involved parameters are given by

$$B_\gamma = 0.011L^2 + 0.14L + 1.3, \quad (15)$$

$$\beta_\gamma = 1/(0.008L^2 + 0.11L + 1.79), \quad (16)$$

$$k_\gamma = 1/(0.014L^2 + 0.049L + 0.801). \quad (17)$$

In addition, it holds $L = \ln(E_p/1000)$. These results are consistent with proton energies in the range of $0.1\,\mathrm{TeV} < E_p < 10^5\,\mathrm{TeV}$. Besides providing $\pi^0$, Eq. (14) also describes the contribution of $\eta$ mesons decay, which is approximately 25% when $x \approx 0.1$.

In the gamma-ray energy range of our interest, $E_\gamma \geq 100\,\mathrm{GeV}$, the gamma-ray emissivity, produced at a distance $z$ along the jet's axis, is given by:

$$Q_\gamma(E_\gamma, z) = cn(z)\int_{\frac{E_\gamma}{E_{max}}}^1 \frac{dx}{x} N_p\left(\frac{E_\gamma}{x}, z\right) \times F_\gamma\left(x, \frac{E_\gamma}{x}\right)\sigma_{pp}^{(inel)}\left(\frac{E_\gamma}{x}\right), \quad (18)$$

where we also make use of the proton energy distribution calculated through Eq. (10) and the inelastic $p-p$ cross-section of Eq. (B.1). Here, $E_{max}$ is the proton maximum energy resulting from Eq. (6). The respective intensity is obtained again through integration over the acceleration zone. For $E_\gamma < 100\,\mathrm{GeV}$, the delta-function approximation is employed.

Finally, integration over the acceleration zone gives the total derived intensity as

$$I_o(E_\gamma) = \int_V Q_\gamma(E_\gamma, z)d^3r = \pi\tan^2\xi\int_{z_0}^{z_{max}} Q_\gamma(E_\gamma, z)z^2 dz. \quad (19)$$

The gamma-ray photons, however, go through various absorption processes that reduce the initially produced intensity $I_o$ to

$$I_\gamma = I_o e^{-\tau}, \quad (20)$$

where $\tau$ denotes the total optical depth of the photon cloud through which the gamma-ray photons pass. We note that the required calculations were performed with the aid of an algorithm developed by our group (in C-language, which employs the Gauss-Legendre numerical integration of the GSL library) and the use of the parameter values listed in Table 1.

## 3. Gamma-ray absorption

As mentioned before, various sensitive telescopes have detected gamma-rays emitted from relativistic collimated jets of BHXRBs. These detectors observe different intensity regions and energy ranges that cover high detection efficiency.

In this subsection, we discuss the gamma-ray absorption due to $e^+ - e^-$ pair production represented by:

$$\gamma + \gamma \rightarrow e^+ + e^-, \quad (21)$$

taking place in the environment of the binary system. The reaction between two photons, the directions of which form an angle $\theta_0$, is shown in Fig. 1. The corresponding cross-section of this reaction is given in Appendix B.2. As can be seen, for gamma-ray photons in the energy range of our interest ($10^2\,\mathrm{GeV} < E_\gamma < 10^7\,\mathrm{GeV}$), a lower energy photon field would be necessary to annihilate them.

**Table 1.** Important parameters that stay constant for all calculations independently of the binary system.

| Parameter | Value | Units |
|---|---|---|
| $\alpha_k$ | 100 | – |
| $q_{rel}$ | 0.1 | – |
| $\eta$ | 0.1 | – |
| $R_c$ | $6\,R_g$ | cm |
| $L_c$ | $5\times10^{36}$ | erg s$^{-1}$ |
| $R_{in}$ | $6\,R_g$ | cm |

### 3.1. Accretion disk absorption

The accretion disk consists of overheated matter and gas rotating together with the system's black hole. The mass accretion rate $\dot{M}_{accr}$ is defined as the rate at which mass from the donor star accumulates onto the equatorial region of the black hole in a binary system. Due to the presence of the magnetic field and high temperature, the disk emits soft X-ray radiation capable of absorbing a portion of the jet-produced energetic photons. In the model employed in this work, the disk is geometrically thin with high optical thickness as described in Cerutti et al. (2011), which follows the disk-$\alpha$ model of Shakura & Sunyaev (1973).

The corresponding optical depth, $\tau_{disk}$, for gamma-ray absorption is given by the integration over the X-ray photon energy, the distance that the high-energy photon travels from the emission source to the observer $l$, and the disk's solid angle (i.e., its radius, $R$, and angle, $\phi$) as:

$$\tau_{disk} = \int_0^\infty\int_0^{2\pi}\int_{R_{in}}^{R_{out}}\int_{\epsilon_{min}}^\infty \frac{dn}{d\epsilon d\Omega}(1-\cos\theta_0) \times\sigma_{\gamma\gamma}\frac{\rho\cos\omega}{D^3}RdRd\phi d\epsilon dl, \quad (22)$$

where $\epsilon_{min} = 2m_e^2c^4/E_\gamma(1-\cos\theta_0)$. The minimum energy range concerning $E_\gamma = 10^2$–$10^7\,\mathrm{GeV}$ is $\epsilon_{min} = 10^{-4}$–$10\,\mathrm{eV}$. In Eq. (22), $\rho$ corresponds to the collision point distance from the central object and D denotes the distance between the disk's surface element and the collision point of the two photons. At the same time, $\omega$ refers to the angle between $\rho$ and the $z$-axis.

The above quantities are connected with the following relations

$$\rho = \left(z^2 + l^2 + 2lz\cos i\right)^{1/2}, \quad (23)$$

$$D = \left(R^2 + \rho^2 - 2R\rho\cos\psi\right)^{1/2}, \quad (24)$$

$$\psi = \cos^{-1}\left(\frac{l\sin i\cos\phi}{\rho}\right), \quad (25)$$

$$\omega = \cos^{-1}\left(\frac{z + l\cos i}{\rho}\right), \quad (26)$$

where, $\psi$ is the angle between the direction of $\rho$ and the disk's radius $R$, while $i$ denotes the angle to the observer's line of sight.

In the aforementioned analysis, for a well-collimated jet (i.e., small half-opening angle $\xi$) in Cartesian coordinates, it holds

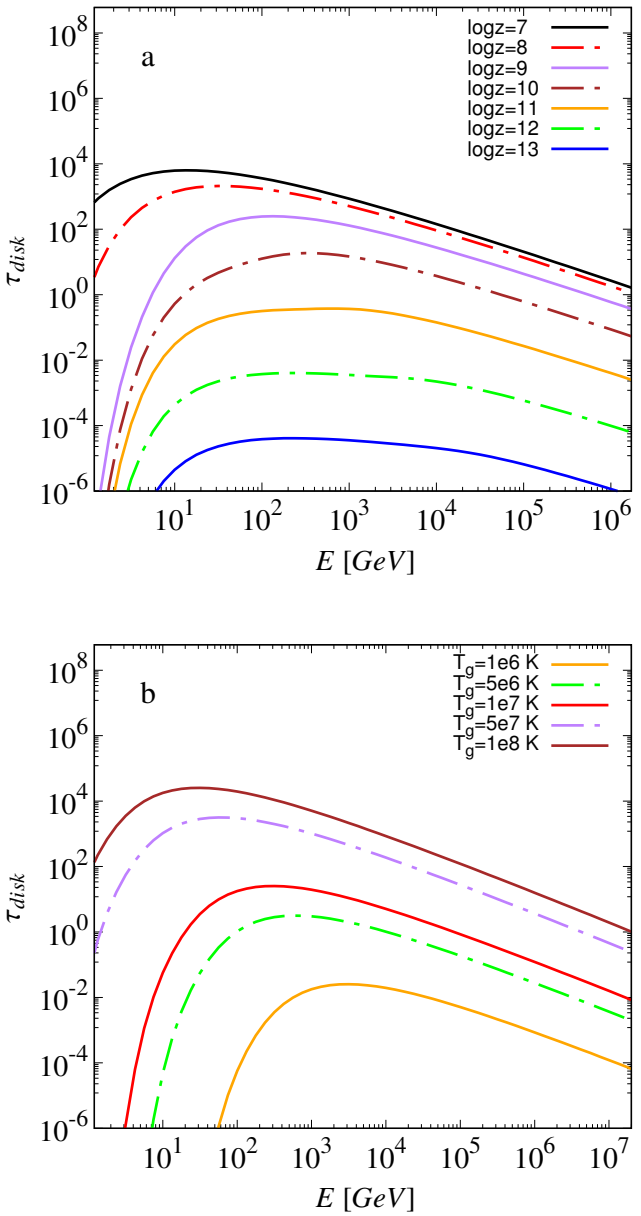


**Fig. 3.** Optical depth for disk absorption in the binary system Cygnus X-1 as a function of gamma-ray photon energy: (a) for different values of $z$ and (b) for different values of inner disk temperature when $z = 5\,R_{\rm Sch}/\tan\xi \approx 10^9$ cm.

$x, y \ll z$. Therefore, only the implication of the $z$-axis of the jet enters our calculations (i.e., $x \simeq y \simeq 0$), see also reference Cerutti et al. (2011). Assuming thermal equilibrium between the infinitesimal surface elements, the emitted photon density by each of them follows the black-body radiation spectrum as

$$\frac{{\rm d}n}{{\rm d}\epsilon {\rm d}\Omega} = \frac{2}{h^3c^3}\frac{\epsilon^2}{e^{\mathcal{T}(R)}-1}, \tag{27}$$

where $\mathcal{T}(R) = \epsilon/k_{\rm B}T(R)$ with $k_{\rm B}$ being the Boltzmann constant (see Table B.1). As can be seen, the temperature depends on the radius $R$. The disk is estimated to begin at the black hole's last stable orbit, which for a stationary object is $R_{\rm in} = R_{\rm ISCO} = 6\,R_{\rm g}$ with $R_{\rm g} = GM_{\rm BH}/c^2$ being the respective gravitational radius. The outer disk radius associated with a donor star that nearly fills its Roche lobe (i.e., by 90%) is approximately $R_{\rm out} \sim 10^{12}$ cm (Eggleton 1983). Beyond that distance, the disk does not contribute much to the absorption in the energy range of our interest.

A realistic temperature dependence on $R$ is given by (Gierliński et al. 1999):

$$T(\bar{r}) = T_{\rm g}\left[\frac{\bar{r}-2/3}{\bar{r}(\bar{r}-2)^3}\left(1-\frac{3^{3/2}(\bar{r}-2)}{2^{1/2}\bar{r}^{3/2}}\right)\right]^{1/4}, \tag{28}$$

where the dimensionless radius is $\bar{r} = R/R_{\rm g}$. The highest temperature closest to the black hole is written as

$$T_{\rm g} = \left(\frac{3GM_{\rm BH}\dot{M}_{\rm accr}}{8\pi\sigma_{\rm SB}R_{\rm g}^3}\right)^{1/4}, \tag{29}$$

where $\sigma_{\rm SB}$ is the Stefan-Boltzmann constant (see Table B.1). The optical depth is primarily sensitive to this temperature, which depends on the system's accretion rate, $\dot{M}_{\rm accr}$. The emission originating from the inner regions of the disk is suitable for lower energy gamma-ray photon annihilation. On the contrary, the outer regional emission tends to absorb higher energy (i.e., >TeV) photons.

In most BHXRBs, the disk total luminosity does not exceed the Eddington limit, $L_{\rm disk} \approx 10^{38}\,{\rm erg\,s^{-1}}$. For this reason, we mainly utilized the approximation: $\dot{M}_{\rm accr} \approx 10^{-8}\,M_\odot\,{\rm yr^{-1}}$. The temperature associated with the innermost stable orbit falls in the range of $T \sim 10^6$–$10^7$ K.

Figure 3 illustrates the calculated optical depth of absorption due to the accretion disk for different distances $z$ from the black hole. As expected, the absorption is much higher for smaller distances of the emission source to the center (Fig. 3a, for $z = 10^7$ cm). It is aptly predicted that a value of $\tau \geq 10^2$ is more than enough to extinguish a substantial part of the gamma-ray emission flux in any system. Seemingly, the emission from the disk loses its dominant role in absorption among its surroundings for greater distances. That is a common characteristic for all energy values presented.

Gamma-ray absorption peaks at energy values that do not surpass $E_\gamma = 10^3$ GeV and then declines inevitably. Disk soft X-ray emission cannot engage in annihilation with the produced gamma-ray photons when $E_\gamma < 1$ GeV while they emerge at $z \geq 10^8$ cm unless the disk's inner region reaches unnaturally high temperatures.

As a second step, we also calculated the optical depth for several values of $T_{\rm g}$ within the presumed range of $10^6$–$10^7$ K, associated with the emission of $\epsilon \sim 1$ keV soft photons. The results are presented in Fig. 3b, in which we notice that greater disk temperatures translate to a significant enhancement in absorption, especially for $T > 1 \times 10^7$ K. More specifically, with an increase in temperature to $T_{\rm g} \approx 5 \times 10^7$ K, the absorption peak becomes three orders of magnitude higher. Of course, the temperature depends on the mass accretion rate (see Eq. (29)), which is mainly considered constant in this case. Even though it could realistically and periodically variate with time, the dynamic interaction between the accretion disk and the system's corona is rather well maintained (Mastichiadis et al. 2022).

The different spectrum phases the system might experience (e.g., as in the case of Cygnus X-1) can be attributed to variations in its mass accretion rate leading to an impact on the unabsorbed gamma-ray flux. We must point out that a slight inaccuracy in the temperature calculation could lead to a substantial deviation in the resulting optical depth.

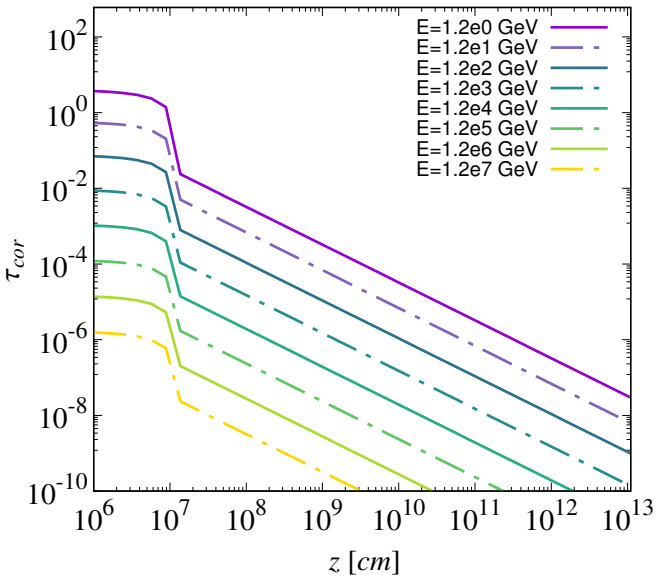


**Fig. 4.** Optical depth for corona absorption in Cygnus X-1 as a function of the distance, $z$, for different values of gamma-ray photon energy.

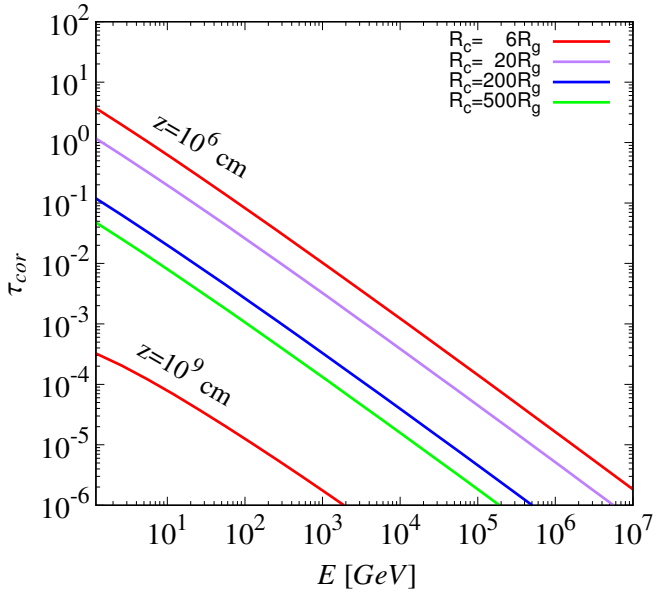


**Fig. 5.** Optical depth for corona absorption in Cygnus X-1 as a function of gamma-ray photon energy for different values of the corona radius given in $R_g$.

### 3.2. Absorption of the black hole's corona

The black hole's corona in an X-ray binary system plays a vital role in many mechanisms capable of altering the energy of particles and photons produced inside or outside the jet. The corona takes a spherical shape around the central object and consists mainly of high-energy electrons which can cool down via synchrotron radiation mechanism or inverse Compton scattering (i.e., by distributing their energy to low-energy photons produced elsewhere in the system).

The corona emission (non-thermal hard X-rays) is of energy range that may absorb high-energy gamma-ray radiation from the jet. Moreover, the optical depth for this interaction, if $z < R_c$, with $R_c$ being the corona radius, would involve two parts. The first corresponds to the case where the gamma-ray photon is still inside the corona (i.e., for $\rho < R_c$), while the second corresponds to the case when the photons escape the corona region (i.e., for $\rho > R_c$) and are heading towards the observer. They are, respectively, written as

$$\tau_{\rm cor}^{\rm in} = \frac{l_0}{2}\int_{\epsilon_{\rm min}}^{\epsilon_{\rm max}}\int_0^{\pi}\frac{{\rm d}n_{\rm in}}{{\rm d}\epsilon}(1-\cos\theta_0)\sigma_{\gamma\gamma}\sin\theta_0{\rm d}\theta_0{\rm d}\epsilon, \quad (30)$$

$$\tau_{\rm cor}^{\rm out} = \int_{l_0}^{+\infty}\int_{\epsilon_{\rm min}}^{\epsilon_{\rm max}}\frac{{\rm d}n_{\rm out}}{{\rm d}\epsilon}(1-\cos\theta_0)\sigma_{\gamma\gamma}{\rm d}\epsilon{\rm d}l. \quad (31)$$

In the above relations, $l$ represents the distance between the collision point and the spot where the photon crosses the corona. The distance $l_0$ between this spot and the source of emission is written as

$$l_0 = \left[R_c^2 - z^2\left(1-\cos^2 i\right)\right]^{1/2} - z\cos i. \quad (32)$$

Furthermore, in Eq. (31), the angle $\theta_0$ between the directions of two colliding photons and the distance $\rho$ between the collision point and the system's black hole are given by

$$\theta_0 = \cos^{-1}\left(\frac{l+l_0+z\cos i}{\rho}\right), \quad (33)$$

$$\rho = \left[(l+l_0)^2 + z^2 + 2z(l+l_0)\cos i\right]^{1/2}. \quad (34)$$

In this work, we adopt the assumption (Cerutti et al. 2011) that the hard X-ray energy density is homogeneous and isotropic inside the spherical region of the corona and descends radially outside the corona. Hence, we have

$$\frac{{\rm d}n_{\rm in}}{{\rm d}\epsilon} = K_0\epsilon^2, \quad (35)$$

$$\frac{{\rm d}n_{\rm out}}{{\rm d}\epsilon} = K_0\left(\frac{R_c}{\rho}\right)^2\epsilon^2, \quad (36)$$

where $K_0$ is the normalization constant that is given in Appendix A.2.

By making use of Eqs. (30) and (31), we calculate and demonstrate in Fig. 4 the total optical depth $\tau_{\rm cor} = \tau_{\rm cor}^{\rm in} + \tau_{\rm cor}^{\rm out}$ and its dependence on $E_\gamma$ and $z$. In both cases, there is an apparent linear dependence on a logarithmic scale. Absorption from the corona becomes increasingly irrelevant as the gamma-ray energy and the source distance from the black hole grows. It peaks at around $\tau_{\rm cor} \approx 5$, far below $\tau_{\rm disk}$ for the same $z$. Admittedly, corona absorption is never the dominant one because, in every $z$, it is overshadowed by either disk or donor star absorption. In Fig. 4, a significant behavior of $\tau_{\rm cor}$ is found for $z = 10^6$–$10^8$ cm when the emission source locates itself inside the corona. In principle, there is a much bigger chance for the photon to be absorbed while traveling inside the corona.

Figure 5 shows the optical depth for several values of the corona radius starting from $R_c = 6\,R_g$. Clearly, for small-scale and more condensed coronas, the absorption is more significant, although the behavior concerning the energy dependence remains unaffected. Beyond a point, further expansion of the coronal sphere shows no significant deviation in the gamma-ray absorption.

### 3.3. Donor star absorption

The binary system's companion star fuels the mass accretion process onto the compact object, yet its contribution is not limited only to the mass. The stellar wind originating from the donor

star has a crucial role in the dynamics of the binary system. It could also penetrate the jet at a higher altitude and provide another $p-p$ interaction mechanism that would result in gamma-ray and neutrino emission (Romero et al. 2007).

In this work, we are primarily interested in the donor star's contribution to gamma-ray absorption, as demonstrated in Böttcher & Dermer (2005). Due to its temperature, the companion star emits thermal black-body radiation that can annihilate higher energy (beyond TeV) gamma-ray photons. In our present study, this is the mechanism with the most dominant role in higher distances from the black hole. The respective optical depth is given by (Böttcher & Dermer 2005):

$$\tau_{\rm donor} = \int_0^{+\infty} \int_{\epsilon_{\rm min}}^{+\infty} \frac{{\rm d}n_{\rm ph}}{{\rm d}\epsilon}(1-\cos\theta_0)\sigma_{\gamma\gamma}{\rm d}\epsilon{\rm d}l, \tag{37}$$

where $\epsilon_{\rm min} = 2m_{\rm e}^2c^4/E_\gamma(1-\cos\theta_0)$. The following expressions provide the angle $\theta_0$, here, and the distance $D$ between the donor star and the collision point

$$\theta_0 = \cos^{-1}\left(\frac{l + z\cos i - s\sin i\cos\alpha}{D}\right), \tag{38}$$

$$D = \left[s^2 + l^2 + z^2 + 2l(z\cos i - s\sin i\cos\alpha)\right]^{1/2}, \tag{39}$$

$$\alpha = \alpha_0 + \frac{2\pi}{P_{\rm orb}}\frac{l}{c}. \tag{40}$$

The system's separation (i.e., the distance between the two stellar components) is indicated by $s$. At the same time, $\alpha - \alpha_0$ is the angular distance the star has covered from its initial phase $\alpha_0$ to the final phase $\alpha$ (i.e., at the moment of emission of the gamma-ray photon to the moment of photon collision at a distance, $l$, from the source).

The radiation field density corresponding to the donor's thermal emission is expressed as

$$\frac{{\rm d}n_{\rm ph}}{{\rm d}\epsilon} = \frac{15}{4\pi^5 c}\frac{L_{\rm star}\mathcal{T}^4}{\epsilon^2 D^2\,(e^{\mathcal{T}}-1)}, \tag{41}$$

where $\mathcal{T} = \epsilon/k_{\rm B}T_{\rm eff}$ is dimensionless and $T_{\rm eff}$ is the donor star's effective surface temperature that depends on its evolutionary phase and stellar type. For a more detailed analysis, the reader is referred to Böttcher & Dermer (2005).

In Fig. 6a, we illustrate the $\tau$ dependence on gamma-ray energy, calculated through Eq. (37). It is evident that the star's contribution to pair production is insufficient compared to the disk. Gamma-ray photons with $E_\gamma < 10\,{\rm GeV}$ remain unaltered, passing through the donor star's emission regardless of the stellar type.

Moreover, the big step from $z = 10^{12}$ to $z = 10^{13}$ cm is remarkable. The system's separation being of similar magnitude to $z$ (i.e., $s \sim 10^{12}$ cm) emerges as the explication. Therefore, separation is no longer dominant in every relation featuring both $z$ and $s$ (i.e., considering smaller distances of the collision points from the source). The drop in absorption for higher $z$ (i.e., nearly $z = 10^{14}$ cm) is not as steep as the respective one in the case of the disk. It becomes apparent that the stellar absorption dominates over the disk one for $z > 10^{10}$ cm. As we show in Sect. 4, this is crucial for the post-absorption gamma-ray intensity graphs.

Additionally, as the photon-emitting source moves further away from the center, the respective energy range (which is gradually affected by the stellar thermal emission) narrows (i.e., for $z > 10^{13}$ cm, it affects photons with $E_\gamma > 100\,{\rm GeV}$).

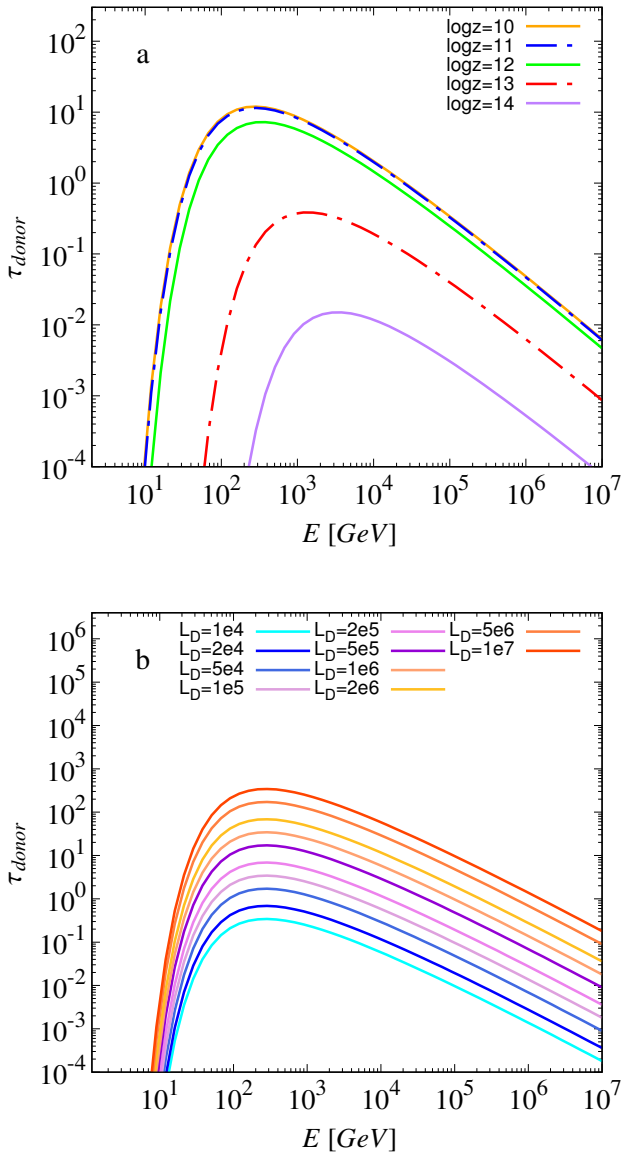


**Fig. 6.** Optical depth for donor star absorption in Cygnus X-1 as a function of gamma-ray photon energy: (a) for different values of $z$ and (b) for different values of donor star luminosity where $L_{\rm D} = L_{\rm star}/L_\odot$ when $z = 5\,R_{\rm Sch}/\tan\xi \approx 10^9$ cm.

Focusing on the functional dependence of Eq. (37), we notice that the donor star's stellar type (i.e., temperature, radius, luminosity) predominantly affects the value of $\tau_{\rm donor}$. For this reason, we plot in Fig. 6b the optical depth as a function of $E_\gamma$ for various orders of magnitude of the donor star's luminosity (given in comparison to solar luminosity). Each order of magnitude correlates with a different stellar type ($A$, $O$, $B$, etc.) associated with the effective stellar temperature. The most common companion stars in binary systems are the supergiants ($O$-type and $B$-type) that belong to the last order of magnitude for $L_{\rm D}$ in Fig. 6. For greater stellar temperatures, $\tau_{\rm donor}$ becomes comparable to $\tau_{\rm disk}$. As in graph (a), the drop is not so steep to be considered negligible for relatively cold stars.

## 4. Results and discussion

The method described in this paper was applied to the Black hole X-ray binary systems: Cygnus X-1, SS 433, and GRS 1915+105.

**Table 2.** Black hole binary systems and their respective parameters used in this work.

| Parameter | Cyg X-1 | SS 433 | GRS 1915+105 | Units |
|---|---|---|---|---|
| $M_{\rm BH}$ | 21.2 | 15 | 12.4 | $M_\odot$ |
| $M_{\rm donor}$ | 40.6 | 21 | 0.5 | $M_\odot$ |
| Type | O | A | K | – |
| $d$ | 2.22 | 5.5 | 8.6 | kpc |
| $i$ | 27.51 | 78.8 | 60 | ° |
| $P_{\rm orb}$ | 5.5998 | 13.082 | 33.85 | days |
| $\dot{M}_{\rm accr}$ | $10^{-8}$ | $10^{-4}$ | $10^{-8}$ | $M_\odot\,{\rm yr}^{-1}$ |
| $L_{\rm star}$ | $3.5\times10^5$ | $3.16\times10^4$ | $10^2$ | $L_\odot$ |
| $T_{\rm eff}$ | 31138 | 8000 | 5000 | K |
| $s$ | $3.65\times10^{12}$ | $5.37\times10^{12}$ | $7.19\times10^{12}$ | cm |
| $u_{\rm b}$ | 0.92 | 0.26 | 0.43 | c |
| $\xi$ | 1.2 | 0.6 | 5 | ° |
| $R_{\rm out}$ | $1.07\times10^{12}$ | $1.69\times10^{12}$ | $4.17\times10^{12}$ | cm |

**Notes.** (1) Cyg X-1, (2) SS 433, (3) GRS 1915+105.
**References.** (1) Miller-Jones et al. (2021), Brocksopp et al. (1999), Stirling et al. (2001), Tetarenko et al. (2019), (2) Bowler (2018), Hillwig et al. (2004), Cherepashchuk (2021), (3) Reid et al. (2014), Steeghs et al. (2013), Punsly & Rodriguez (2016).

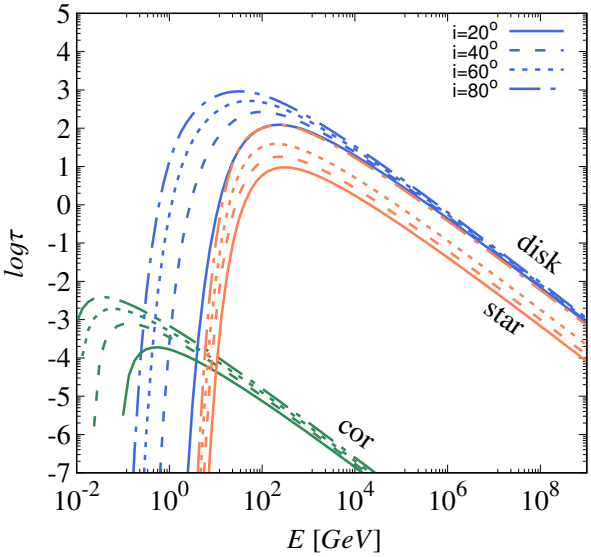


**Fig. 7.** Optical depth for all kinds of absorption for varying inclinations of Cygnus X-1 when $z = 5\,R_{\rm Sch}/\tan\xi \approx 10^9$ cm.

These systems were chosen on the basis of the richness of their observations and their relatively small distances from Earth (2−8 kpc), as well as some existing theoretical studies focused. These systems have different companion star types (i.e., *O*-, *A*- and *K*-type, respectively) that indicate the impact of the donor star's absorption on the emitted gamma-ray intensities. The system parameters used in our present calculations are listed in Table 2.

We note that for SS 433 and GRS 1915+105, explicit star surface temperatures and luminosities are not quoted in the bibliography; thus, for our purposes, we implement the values that most likely fit their spectral analysis and stellar type assumptions. The donor star of SS 433 is a cooler type A supergiant (Hillwig et al. 2004), while the GRS 1915+105 has a much smaller *K*-type giant that appears in the hotter region of the Hertzsprung-Russell diagram (Reid et al. 2014).

Furthermore, we compared our results with gamma-ray observations for the aforementioned BHXRB systems, focusing on the VHE regime. We should point out, however, that most gamma-ray telescopes are optimized for measurements below $E_\gamma \approx 10$ TeV. Therefore, detection signals beyond this energy are unlikely to be recorded, although some telescopes, such as HAWC, are aimed at this purpose.

### 4.1. Cygnus X-1

Cygnus X-1 is one of the brightest X-ray Galactic sources detectable from the Earth and the first source to have been broadly accepted as a BHXRB. It was initially believed to be located at a distance of 1.86 kpc from the Earth (Reid et al. 2011), but recently the distance was reassessed by Miller-Jones et al. (2021) to be at 2.22 kpc. In addition, new estimations have led to the revision (see Table 2) of the mass predictions by Orosz et al. (2011). The system's companion star is the type O blue supergiant HDE 226868 and has a nearly circular orbit (it never eclipses). At the same time, the mass transfer from the donor to the accretion disk is greatly facilitated by the donor's stellar wind (see Table 2 for more parameter values). Moreover, Cygnus X-1 is the most persistent and brightest source of hard X-ray emission (i.e., $\epsilon > 30$ keV). These photons are probably produced by the inner parts of the accretion disk and boost their energy through Compton scattering with corona electrons or reflection from the disk's surface.

Recently, a debate was provoked by Krawczynski et al. (2022) regarding the system's angle to the line of sight and the question of whether it is indeed above 45°. This led to Zdziarski & Egron (2022) adopting both values (i.e., $i = 27°$ and 45°) for the purposes of their study. In order to cover all possibilities, we calculated the optical depths for all kinds of absorption for varying inclinations (Fig. 7). Most importantly, greater angles increase pair production and the energy range of affected photons by shifting the respective cutoff towards lower energies.

A notable characteristic of the system is that it demonstrates two highly distinct X-ray states, namely, the hard and the soft. The hard X-ray state is the most common where the system spends most of the time and is associated with stable jets and a strong, compact corona responsible for the X-ray spectrum's hardening. On the other hand, the soft state is accompanied by broader spectrum variability attributed to the transitional phase of the corona regeneration process (Fender et al. 2004). In this state, radio emission is not detected (Brocksopp et al. 1999). There is also an intermediate state with a really short duration on the order of a few days. The system's jets extend up to a distance of $z = 10^{19}$ cm (Gallo et al. 2005).

In this work, we calculated gamma-ray intensities emitted from the Cygnus X-1, along with the effects of absorption mechanisms. More specifically, in Fig. 8, we present the results for two different values of $z$ ($z = 10^7$ and $z = 10^{10}$ cm), showing the impact of the absorption of the disk, corona, and donor star on gamma-ray emission produced inside the jet. As is evident from Fig. 8a, the disk vastly dominates and shapes the $I_\gamma$ curve for lower $z$ values. That can be verified by glancing at the respective optical depth graphs in the previous sections. The corona, nonetheless, does not affect the emission. However, being injected by all these spare $e^+e^-$ pair-products of photon annihilation (i.e., from other kinds of absorption as well) could lead to its significant reinforcement.

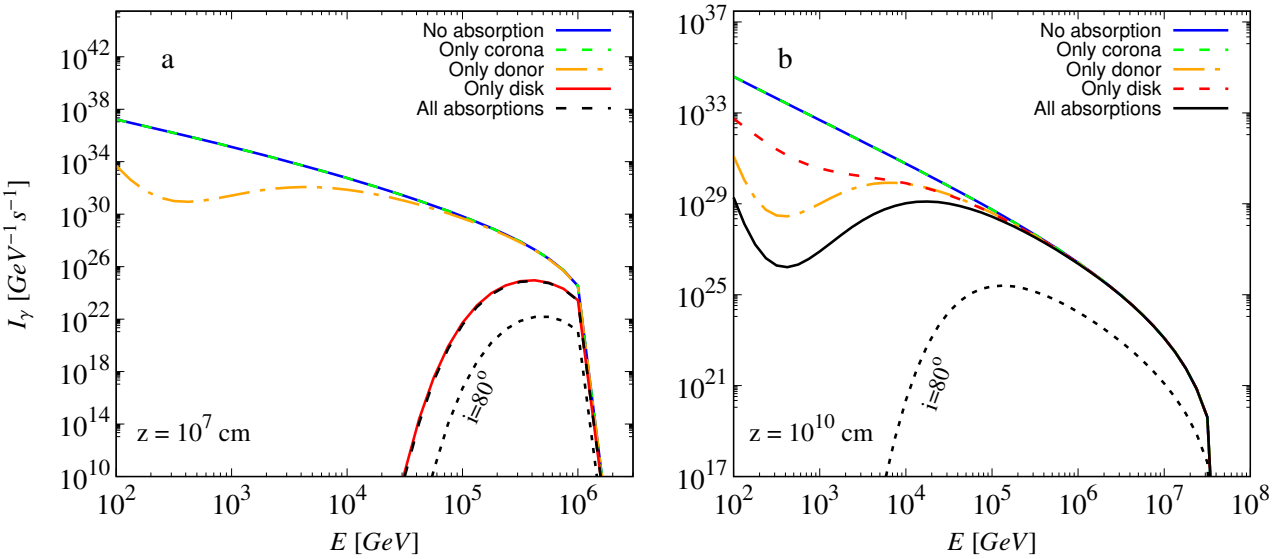


**Fig. 8.** Gamma-ray intensity emitted by Cygnus X-1 as a function of photon energy for (a) $z = 10^7$ cm and (b) $z = 10^{10}$ cm. The solid line (blue) corresponds to the obtained intensity by ignoring all types of absorption, while the dashed line refers to an intensity affected only by corona absorption. The dash-dotted line (orange) represents gamma-ray intensity exposed only to the donor star's radiation. A red solid (or dashed) line demonstrates intensity post-absorption from the accretion disk. Finally, gamma-ray intensity, including all the discussed absorption mechanisms, is represented by the black dashed (or solid) line.

The donor star's thermal radiation absorbs mostly lower energy gamma-ray photons of $\sim 10^3$ GeV. For $z = 10^7$ cm, the donor's impact is greatly minimized by the superiority of the disk's soft X-ray density. The final intensity at its peak (it occurs for $E_\gamma = 3 \times 10^5$ GeV) formed by photons escaping the disk photons consists of only 0.01% of the respective non-absorption intensity. Notably, the lower energy gamma-ray intensity is highly attenuated for smaller distances.

In Fig. 8b, which corresponds to a significantly higher source distance ($z = 10^{10}$ cm) from the black hole, we see that a substantial decline mainly in the disk's contribution to higher energy photon annihilation occurs that holds especially for $E_\gamma > 10^3$ GeV. The gamma-ray photon production reduces with the distance but not notably. The conclusion is that for $z > 10^{10}$ cm, the donor star is taking over from the disk in shaping the gamma-ray intensity curve. The aforementioned curve is shifted down as it is not yet utterly unaffected by the accretion disk's optically thinner photon density. For $E_\gamma > 10^5$ GeV, the intensity remains unaffected.

Figure 8 also presents the respective post-absorption intensities corresponding to a very high system inclination (i.e., $i = 80°$). Therefore, smaller angles shall dictate gamma-ray intensity curves in between (i.e., the black lines in graphs a and b). Greater alignment with the jet axis diminishes the photon annihilation efficiency (see graph b). It also offers a better opportunity to study jet mechanics combined with amplified Doppler boosting.

The difference regarding the maximum gamma-ray energy is attributed to more intense energy-loss interactions of the relativistic protons inside the jet. As mentioned in Sect. 2, $E_{\max}$ depends on the sign between the energy-gain (*Fermi* acceleration) and the energy-loss rates due to particle collisions, synchrotron emission, and so on.

### 4.2. SS 433

The SS 433 is a Galactic XRB located at a distance of 5.5 kpc from Earth (Romney et al. 1987). The system's companion star is an *A*-type, relatively cool supergiant (see Table 2) with a slightly eccentric orbit around the central object with a period that seems to increase marginally with time (Cherepashchuk et al. 2021). This is a strong indication that the central object is, in fact, a black hole, clarifies prior ambiguities among the community as to whether the central object is a neutron star instead of a black hole.

The SS 433 is one of the most exotic binary systems, known for the fact that it does not preserve a constant inclination angle, instead precessing with a 162.25 day-period over a 20° cone around an axis. The angle between the axis and the line of sight is given in Table 2 (Cherepashchuk 2021). In most similar sources, jets are only occasionally observed. However, in SS 433, they persist over many years with no apparent velocity variation, which is possibly due to the system's super-Eddington accretion limit. In addition, the supergiant companion star transfers mass at an incredibly high rate to the black hole, which is also the reason for the significant presence of a wind coming from the accretion disk. It has also been suggested that SS 433 is an ultra-luminous X-ray source (i.e., ULX), as viewed from the outflow axis (Begelman et al. 2006).

Furthermore, the system's jets extend at very large distances from the center ($z \approx 10^{20}$ cm). This is due to the supercritical accretion rate that results in very high jet collimation (small half-opening angle). In addition, many observations and spectral analyses verify the existence of baryonic content in the system's jets, which qualifies it as a concrete example where the hadronic model can be applied (Reynoso et al. 2008; Ahnen et al. 2018).

In Figs. 9a,b, we demonstrate the gamma-ray intensities produced in SS 433 and then subject to different origins of absorption. They refer to two distinct values of $z$, as done in the case of Cygnus X-1. Graph a clearly shows the lack of gamma-ray emission after absorption from the disk. Gamma-ray radiation is extinct for $z < 10^7$ cm, which is due to the system's super-Eddington accretion limit (Fabrika 2004), as shown in Table 2. The unusually high $\dot{M}_{\rm accr}$ of SS 433 drastically increases the disk's temperature $T_{\rm g}$ and, simultaneously, the opacity of the soft X-ray photon density emitted. The respective optical depth

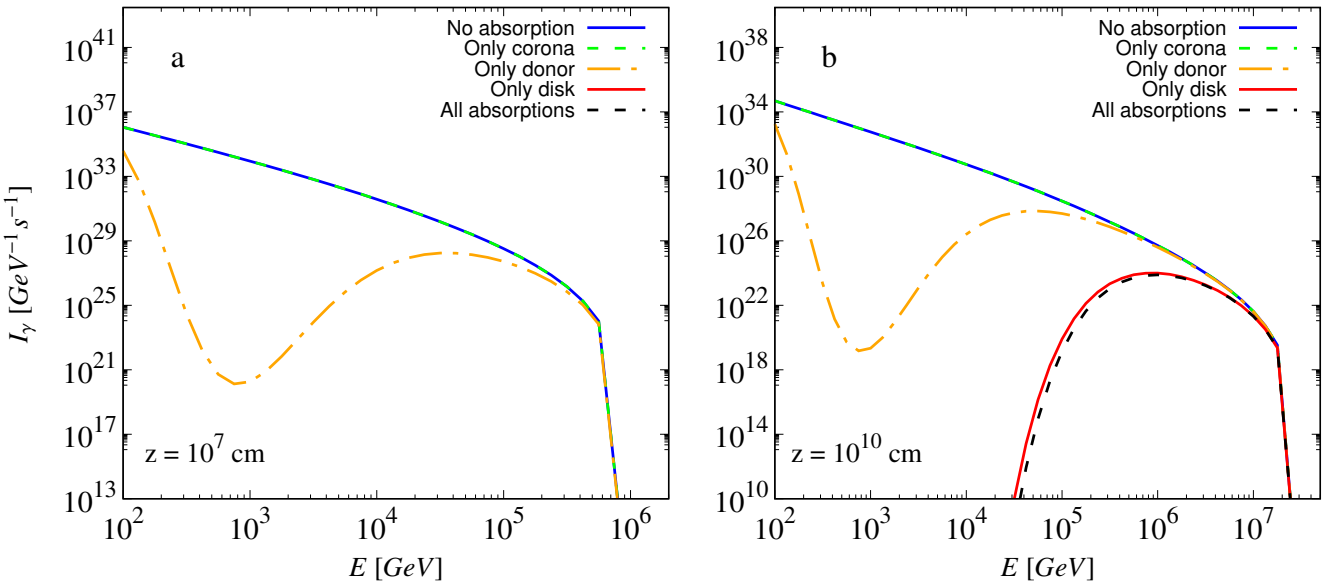


**Fig. 9.** Gamma-ray intensity emitted by system SS 433 as a function of photon energy for (a) $z = 10^7$ cm and (b) $z = 10^{10}$ cm. The line colors and types are the same as the respective graphs for Cygnus X-1.

increases by 2−3 orders of magnitude, enough to annihilate any nearby high-energy photon.

Regarding the donor star absorption, we notice the increased steepness of the corresponding curve as compared to Cygnus X-1 and the more considerable depth in an extensive energy range compared to the former. However, considering the cooler star in SS 433, we would expect the opposite, but the higher inclination (79° to 30°) seems to have a more significant impact on determining the final intensity curve assuming similar stellar luminosity.

Increasing the source distance from the compact object by three orders of magnitude (i.e., $z = 10^{10}$ cm), the disk's involvement decisively reduces the intensity (see Fig. 9b). Actually, the gamma-ray radiation survives for $E_\gamma > 10^4$ GeV. Concerning the corona's impact, it is not very important, as in the case of the Cygnus X-1 system. Of course, it relates to the assumption that most corona parameters are constant in our calculations (see Table 1). As can be seen from Fig. 5, even altering these parameters would have no noticeable impact. Instead, with higher $z$, the corona is proven to be increasingly irrelevant to the total absorption, which could potentially change by considering other energy-altering mechanisms that might contribute to an optically thicker corona. In brief, gamma-ray absorption is dominant for $E_\gamma < 10^3$ GeV in the lower jet regions, however, below a specific value of disk temperature, lower energy emission ($E_\gamma < 500$ MeV) is possible from the base of the jet (Rasul et al. 2019). Regarding higher energy gamma-ray emission, it is certainly not ruled out with respect to observations, as seen in Fig. 9.

### 4.3. GRS 1915+105

The GRS 1915+105 system is a BHXRB located at a distance of 8.6 kpc in our Galaxy (Reid et al. 2014) that hosts a medium-sized black hole and a low-mass companion star (see Table 2) which is a $K1$-type giant (Steeghs et al. 2013). This system has some characteristics that make it unique. First, it has the longest orbital period ever observed among low-mass XRBs (Steeghs et al. 2013). This results in the largest accretion disk size-wise that constitutes a huge mass supplier to the compact object. The GRS 1915+105 was the first source in the Galaxy to exhibit apparent super-luminal motion of its relativistic jets (Mirabel & Rodríguez 1994).

The system used to emit consistently 10%−100% of its Eddington luminosity in the X-ray band. In 2018, however, it experienced an outburst that caused a drop of nearly an order of magnitude concerning the total luminosity. General alterations followed it regarding its flaring activity and accretion states. As a result, GRS 1915+105 has descended into a low-luminosity hard X-ray state that is assumed to end in the near future. Moreover, the system constitutes a perfect example for studying the accretion process and the geometrical properties of an accretion disk due to its vast size and convenient angle to the line of sight (Koljonen & Hovatta 2021).

In Fig. 10, we illustrate the gamma-ray intensities produced in the relativistic jets of GRS 1915+105. The most notable difference compared to previous black hole binary systems is the negligible influence of the donor star on the gamma-ray emission curve. That is due to the star's temperature (as a $K$-type giant; see Table 2), which is comparably small. Eventually, the emission from the accretion disk is the only one that absorbs high-energy photons from the jet. Since the system's accretion disk is unusually large, photons from its outer regions mostly annihilate the higher energy-band photons compared to the inner disk regions. Nonetheless, for $R_{\rm out} > 10^{10}$ cm, the impact on the optical depth is insignificant. For $z \approx 10^7$ cm, the only gamma-ray photons that survive belong to the range $E_\gamma = 10^5$−$10^6$ GeV, just as in the case of Cygnus X-1 (both having similar accretion rates).

### 4.4. Gamma-ray emitted integral fluxes

The respective gamma-ray integral fluxes emitted from the systems discussed in this work are calculated via the relation:

$$\Phi_\gamma = \int_{100}^{E_{\rm max}} \frac{I_\gamma(E_\gamma)\mathrm{d}E_\gamma}{4\pi d^2}, \tag{42}$$

where $d$ denotes the distance to the Earth of the studied system (see Table 2).

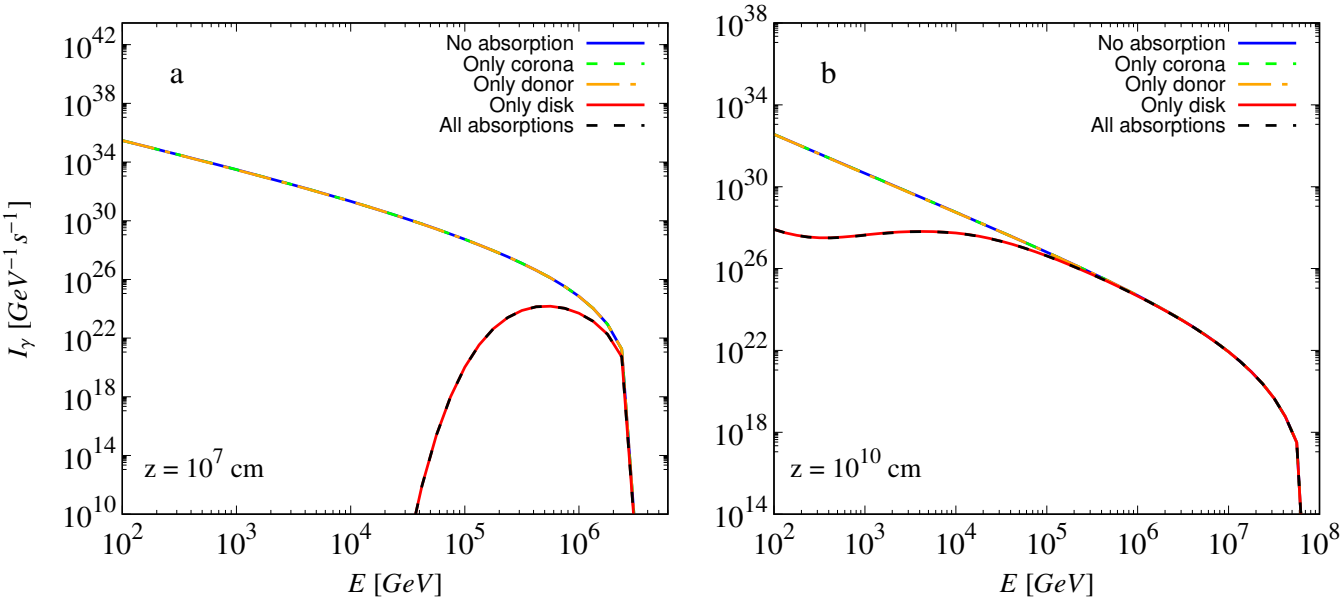


**Fig. 10.** Gamma-ray intensity emitted from the GRS 1915+105 system as a function of photon energy for (a) $z = 10^7$ cm and (b) $z = 10^{10}$ cm. The line colors and types are the same as the graphs for Cygnus X-1 and SS 433.

In Fig. 11, we show the integral fluxes emitted from the binary systems: Cygnus X-1, SS 433, and GRS 1915+105 for various particle acceleration distances measured from the center of the compact object (black hole). Specifically, we demonstrate the respective integral fluxes before and after the absorption process in order to emphasize the effect of the system's surroundings on the emission detection possibilities. The initial fluxes resolve in a declining linear behavior related to the conic-like jet shape.

All the relevant cooling mechanisms that determine the maximum proton energy and shape the corresponding particle distributions decline massively with the jet expansion (i.e., due to a decrease in cold proton density) and become irrelevant. The result is that the value of $E_{\rm max}$ is stabilized for $z > 10^{13}$ cm. In addition, the acceleration mechanism grows more inefficient with the distance from the center. In order to uphold the gamma-ray production process for $z > 10^{10}$ cm, other mechanisms should also make a contribution, such as the ones described by the leptonic models or a more strictly collimated jet. In the same graph, we plot the upper limits for each system we discuss in Sect. 1, for comparison.

As implied from Fig. 11, the system with the highest gamma-ray flux (even after absorption) is the Cygnus X-1, which maintains a relatively high flux from the most significant part of the jet's length. Only for $z \approx 10^{11}$ cm occurs an evident decrease attributed to the donor star radiation that takes over the absorption process combined with the drop in gamma-ray production rate. When the corresponding optical depth also reduces significantly, the gamma-ray flux increases. These results are consistent with those of Zanin et al. (2016), concluding that the emission region is constrained to $z = 10^{11}$–$10^{13}$ cm since disk absorption is weak enough at those distances and the donor star emission cannot absorb efficiently for $E_\gamma < 20$ GeV. Furthermore, our results exceed the 95% CL (i.e., confidence level) upper limit of $\Phi_\gamma < 2.6 \times 10^{-12}$ ph cm$^{-2}$ s$^{-1}$ for $E_\gamma > 200$ GeV (Ahnen et al. 2017). However, we employed a relatively high value for the portion of relativistic particles inside the jet (i.e., $q_{\rm rel}$).

On the contrary, SS 433 does not exhibit sufficient photon flux for $z < 10^{10}$ cm due to the disk absorption, as seen in Fig. 9.

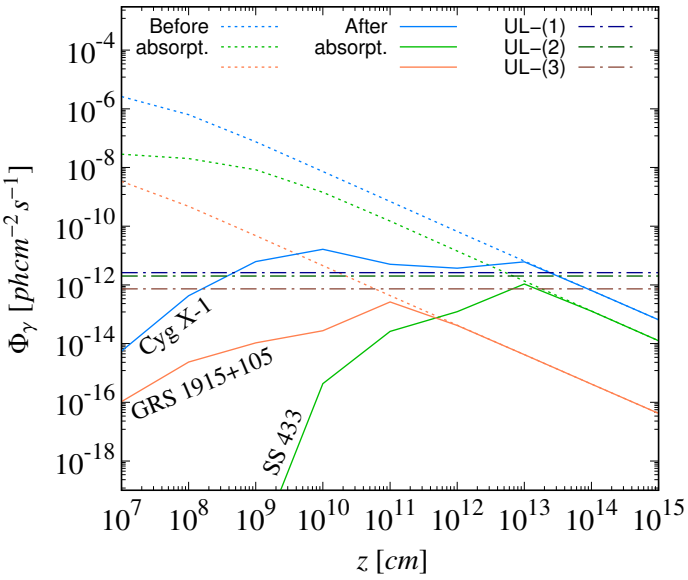


**Fig. 11.** Gamma-ray integral fluxes for various distances $z$ for binary systems Cygnus X-1, SS 433, and GRS 1915+105. The dashed lines correspond to emissions not affected by absorption from the system's surroundings. In contrast, the solid lines represent the gamma-ray fluxes after absorption from the accretion disk, corona, and donor star. The fluxes are integrated for $E_\gamma \geq 10^2$ GeV. The upper limits among the three systems are also demonstrated as: (1) Cygnus X-1, Ahnen et al. (2017), (2) SS 433, Ahnen et al. (2018), (3) GRS 1915+105, Abdalla et al. (2018).

For greater distances, however, the behavior of the integral flux is similar to the respective Cygnus X-1 flux, which agrees with the findings of Bordas et al. (2010), regarding the emission from $z \geq 10^{13}$ cm. Our predictions for SS 433 are in agreement with the 99% CL upper limit of $\Phi_\gamma < 2 \times 10^{-12}$ ph cm$^{-2}$ s$^{-1}$ set by Ahnen et al. (2018) for $E_\gamma > 300$ GeV. Specifically, it is only for $z = 10^{13}$ cm that the integral flux comes close to it.

Finally, gamma-rays from the jets of GRS 1915+105 are hardly detectable. This is attributed to the greater half-opening

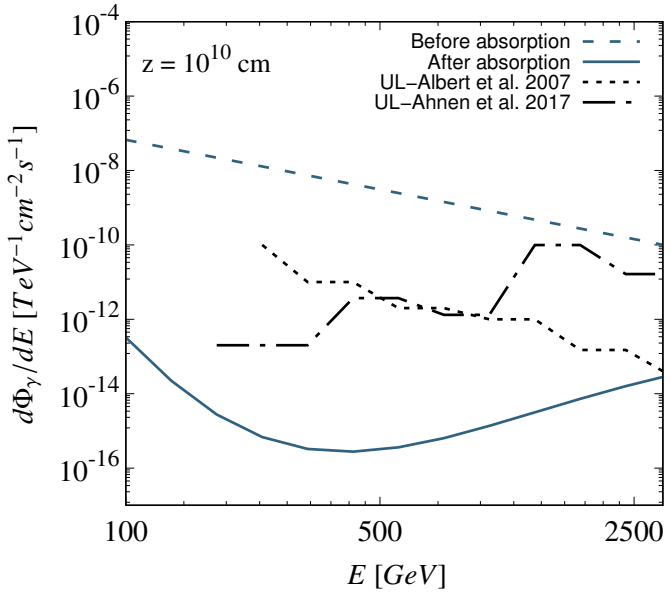


**Fig. 12.** Differential flux for gamma-rays emitted from the jets of Cygnus X-1 at $z = 10^{10}$ cm. The 95% CL upper limits of Albert et al. (2007) and Ahnen et al. (2017) are also plotted. They refer to power-law spectra with a photon index of $\Gamma = 3.2$.

angle (see Table 2) and system inclination. Comparisons with the established upper limits, such as the 99.9% CL $\Phi_\gamma < 0.61 \times 10^{-12}$ ph cm$^{-2}$ s$^{-1}$ of Acero et al. (2009) for $E_\gamma > 410$ GeV and the respective 99% CL limit $\Phi_\gamma < 7.3 \times 10^{-13}$ ph cm$^{-2}$ s$^{-1}$ for $E_\gamma > 560$ GeV by Abdalla et al. (2018) verify our results as can be seen in Fig. 11. Although they were estimated based on a more restricted photon energy range (>400 GeV), the less-energetic photons that would otherwise contribute most to the integral fluxes are those that are mostly annihilated. The integral fluxes presented in this work may be assumed as the upper limits for gamma-ray emissions due to the relatively high free-parameter values implemented.

In Fig. 12, we calculate the corresponding differential fluxes before and after absorption for Cygnus X-1 at a distance $z = 10^{10}$ cm. The distance was chosen based on the peak integral counterpart of Fig. 11. The comparison with the 95% CL ULs (i.e., upper limits) of Albert et al. (2007) and Ahnen et al. (2017) indicates that absorption plays an integral role in the unsuccessful attempts at detection of VHE emission from Cygnus X-1. The same could also be insinuated for SS 433 and GRS 1915+105. That holds for the low-inclination case where the optical depth is reduced. Otherwise, the differential flux would be much lower.

Here, we assume a highly efficient jet concerning particle acceleration. However, in a more realistic scenario, the photon production rate could not produce fluxes well above the established upper limits. That leaves the upper jet regions and their interaction with the interstellar medium the only viable solution for producing detectable VHE emission. Indeed, there was detection of such emission localized in the lobes of SS 433 (Abeysekara et al. 2018) attributed to magnetically accelerated electrons.

Predictions of the incoming gamma-ray flux from SS 433 by Reynoso et al. (2008) indicate a high value of $\Phi_\gamma \approx 10^{-11}$ ph cm$^{-2}$ s$^{-1}$. Although they implemented a much lower value of $q_{\rm rel} = 10^{-4}$, the flux dependence on it is linear on a logarithmic scale. Therefore, adjusting those predictions to our parameter values would fit our $z = 10^9$ cm estimation of Fig. 11 without considering photon absorption (when the precessional phase nears 0 or 1). However, we predict a much lower photon flux after absorption from the disk because of the integration over the whole disk surface, including the highly heated innermost regions.

Cygnus X-1 emission was modeled by Kantzas et al. (2020) using a multi-zone lepto-hadronic model. Their study was focused, however, on lower energy emissions in order to explain the observational data and, thus, do not include absorption effects given the circumstantial conditions of the observations. The same holds for the proposed 2D time-dependent radiation model by Zhang et al. (2014) that focuses on lepton acceleration through a first-order *Fermi* mechanism. It refers to higher jet emission regions (i.e., $z > 10^{11}$ cm) neglecting disk absorption.

## 5. Summary and conclusions

Galactic stellar black hole X-ray binaries are some of the most exotic and compelling astrophysical systems consisting of a central compact object (stellar black hole or a neutron star) in a common orbit with a companion (donor) star (often a giant or supergiant star). Due to the strong gravitational attraction, mass, and gas are extracted from the companion star and accumulate around the compact object, thus forming an overheated X-ray source in the form of an accretion disk. At the same time, plasma outflows are ejected in the form of two opposite collimated and accelerated jets perpendicularly to the plane of the disk. The jets can be ejected to distances $z > 10^{17}$ cm.

Finally, due to an interaction with the interstellar medium, they are resolved in two radio lobes that appear uniquely distinct in the observations. Moreover, the bulk-like jets are being accelerated to relativistic velocities and, with the right system inclination, can be traced back to Earth, where spectral detection and analysis are possible. These systems function as Galactic particle accelerators and multi-wavelength emitters. Inside the jets, further particle acceleration is possible in zonal regions of the jet through shock-waves (second *Fermi* mechanism) that produce highly energized distributions of electrons and protons.

In this work, based on established lepto-baryonic models where accelerated protons collide with the thermal protons of the jet, we attempted to calculate the gamma-ray emission from the systems mentioned above. The proton-proton scattering produces secondary particles: pions, kaons, etas, and muons. Their decay leads to the emission of neutrinos and gamma-ray photons that reach the Earth's detectors. Our primary focus is calculating gamma-ray intensities originating from neutral pion decay and considering the influences of the disk, the corona, and the donor star on these intensities. Each of the latter components emits lower energy photons (soft and hard X-rays), capable of absorbing gamma-rays during their journey from the source point inside the jet to the terrestrial detector.

We also calculated the optical depths for absorption due to the disk, corona, and donor star emission for various source distances from the black hole center. In addition, we explored the dependence of each absorption type on the most sensitive parameters (disk temperature, corona radius, and donor's stellar type). Then, we applied the absorption effects on the gamma-ray intensities produced in three concrete BHXRB examples, namely, Cygnus X-1, SS 433, and GRS 1915+105.

From the above investigation, we conclude that the disk absorption dominates over source distances up to $z \approx 10^{10}$ cm from the black hole. For $10^{10} < z < 10^{12}$ cm, the donor star absorption takes over unless there is an unusually high mass

accretion rate, as in SS 433, or there is a much greater binary separation. Beyond this point ($z \geq 10^{13}$ cm), the absorption effect of the donor star decreases radically but remains the dominant one over the corona and mainly over the disk one as well. The absorption overall decreases with the distance from the black hole, as does the gamma-ray production.

The Cygnus X-1 presents the highest gamma-ray integral flux from the individual binary systems studied, with relatively weak disk absorption and sufficient donor emission. On the other hand, the GRS 1915+105 emits the least radiation, while it presents the weakest absorption due to both the disk and the donor star. The reason is the angle to the line of sight and the jet's half-opening angle in Table 2. However, the latter is a dubious parameter that cannot be easily determined. Considering the lack of VHE observations that cannot be attributed to absorption, an insufficiency in terms of gamma-ray production is possible. Concerning the SS 433, this system is subjected to the most substantial absorption, mainly due to its super-Eddington accretion rate and inclination in the case of donor star absorption. Despite that, SS 433 is a more powerful emitter in the VHE regime than the GRS 1915+105 for distances $z > 10^{11}$ cm from the compact object. Notably, from a quantitative point of view, we may consider several other mechanisms contributing to the total gamma-ray emissivity. Our results, however, have great qualitative value when focusing on the dominant gamma-ray emission and absorption mechanisms that are assumed.

*Acknowledgements.* The author Th.V. Papavasileiou wishes to thank T.S. Kosmas for fruitful discussions and A. Papavasileiou for technical assistance.

## References


Abdalla, H., Abramowski, A., Aharonian, F., et al. 2018, A&A, 612, A10
Abeysekara, A. U., Albert, A., Alfaro, R., et al. 2018, Nature, 562, 82
Acero, F., Aharonian, F., Akhperjanian, A. G., et al. 2009, A&A, 508, 1135
Achterberg, A., Gallant, Y. A., Kirk, J. G., & Guthmann, A. W. 2001, MNRAS, 328, 393
Aharonian, F., Akhperjanian, A., Beilicke, M., et al. 2005, A&A, 439, 635
Ahnen, M., Ansoldi, S., Antonelli, L., & Arcaro, C. 2017, MNRAS, 472, 3474
Ahnen, M. L., Ansoldi, S., Antonelli, L. A., et al. 2018, A&A, 612, A14
Albert, J., Aliu, E., Anderhub, H., et al. 2007, ApJ, 665, L51
Begelman, M. C., Rudak, B., & Sikora, M. 1990, ApJ, 362, 38
Begelman, M. C., King, A. R., & Pringle, J. E. 2006, MNRAS, 370, 399
Bodaghee, A., Tomsick, J. A., Pottschmidt, K., et al. 2013, ApJ, 775, 98
Bordas, P., Bosch-Ramon, V., & Paredes, J. M. 2010, Int. J. Mod. Phys. D, 19, 749
Bosch-Ramon, V., Romero, G. E., & Paredes, J. M. 2006, A&A, 447, 263
Böttcher, M., & Dermer, C. D. 2005, ApJ, 634, L81
Bowler, M. G. 2018, A&A, 619, L4
Brocksopp, C., Fender, R. P., Larionov, V., et al. 1999, MNRAS, 309, 1063
Cerutti, B., Dubus, G., Malzac, J., et al. 2011, A&A, 529, A120
Cherepashchuk, A. 2021, Space Sci. Rev., 102, 23
Cherepashchuk, A. M., Belinski, A. A., Dodin, A. V., & Postnov, K. A. 2021, MNRAS, 507, L19
Eggleton, P. P. 1983, ApJ, 268, 368
Fabrika, S. 2004, Astrophys. Space Phys. Rev., 12, 1
Fender, R. P., Belloni, T. M., & Gallo, E. 2004, MNRAS, 355, 1105
Gallant, Y. A., & Achterberg, A. 1999, MNRAS, 305, L6
Gallo, E., Fender, R., Kaiser, C., et al. 2005, Nature, 436, 819
Gierliński, M., Zdziarski, A. A., Poutanen, J., et al. 1999, MNRAS, 309, 496
Gould, R. G., & Schréder, G. P. 1967, Phys. Rev., 155, 1404
Hillwig, T. C., Gies, D. R., Huang, W., et al. 2004, ApJ, 615, 422
Kantzas, D., Markoff, S., Beuchert, T., et al. 2020, MNRAS, 500, 2112
Kelner, S. R., Aharonian, F. A., & Bugayov, V. V. 2006, Phys. Rev. D, 74, 034018
Khangulyan, D., Hnatic, S., Aharonian, F., & Bogovalov, S. 2007, MNRAS, 380, 320
Kirk, J. G., Guthmann, A. W., Gallant, Y. A., & Achterberg, A. 2000, ApJ, 542, 235
Koljonen, K. I. I., & Hovatta, T. 2021, A&A, 647, A173
Körding, E. G., Fender, R. P., & Migliari, S. 2006, MNRAS, 369, 1451
Kosmas, O., & Smponias, T. 2018, Adv. High Energy Phys., 2018, 9602960
Krawczynski, H., Muleri, F., Dovčiak, M., et al. 2022, Science, 378, 650
Marshall, H. L., Canizares, C. R., & Schulz, N. S. 2002, ApJ, 564, 941
Mastichiadis, A., Petropoulou, M., & Kylafis, N. D. 2022, A&A, 662, A118
Miller-Jones, J. C. A., Bahramian, A., Orosz, J. A., et al. 2021, Science, 371, 1046
Mirabel, I. F., & Rodríguez, L. F. 1994, Nature, 371, 46
Orosz, J. A., McClintock, J. E., Aufdenberg, J. P., et al. 2011, ApJ, 742, 84
Papavasileiou, T., Kosmas, O., & Sinatkas, I. 2021a, Galaxies, 9, 67
Papavasileiou, T. V., Papadopoulos, D. A., & Kosmas, T. S. 2021b, J. Phys.: Conf. Ser., 1730, 012138
Papavasileiou, T., Kosmas, O., & Sinatkas, I. 2022, Symmetry, 14, 485
Punsly, B., & Rodriguez, J. 2016, ApJ, 823, 54
Rasul, K., Chadwick, P. M., Graham, J. A., & Brown, A. M. 2019, MNRAS, 485, 2970
Reid, M. J., McClintock, J. E., Narayan, R., et al. 2011, ApJ, 742, 83
Reid, M. J., McClintock, J. E., Steiner, J. F., et al. 2014, ApJ, 796, 2
Reynoso, M. M., & Carulli, A. M. 2019, Astropart. Phys., 109, 25
Reynoso, M. M., & Romero, G. E. 2009, A&A, 493, 1
Reynoso, M. M., Romero, G. E., & Christiansen, H. R. 2008, MNRAS, 387, 1745
Romero, G. E., Torres, D. F., Kaufman Bernadó, M. M., & Mirabel, I. F. 2003, A&A, 410, L1
Romero, G. E., Okazaki, A. T., Orellana, M., & Owocki, S. P. 2007, A&A, 474, 15
Romero, G. E., Boettcher, M., Markoff, S., & Tavecchio, F. 2017, Space Sci. Rev., 207, 5
Romney, J. D., Schilizzi, R. T., Fejes, I., & Spencer, R. E. 1987, ApJ, 321, 822
Saito, T. Y., Zanin, R., Bordas, P., et al. 2009, Contribution to the 31st ICRC, Lodz, Poland
Schüssler, F., Bordas, P., Chadwick, P. M., Dickinson, H., & Ernenwein, J. P. 2015, Proceedings of the 34th International Cosmic Ray Conference (ICRC2015)
Shakura, N. I., & Sunyaev, R. A. 1973, A&A, 24, 337
Smponias, T., & Kosmas, T. S. 2011, MNRAS, 412, 1320
Smponias, T., & Kosmas, T. S. 2013, MNRAS, 438, 1014
Steeghs, D., McClintock, J. E., Parsons, S. G., et al. 2013, ApJ, 768, 185
Stirling, A., Spencer, R., de La Force, C., et al. 2001, MNRAS, 327, 1273
Szostek, A., Dubus, G., Brun, F., & de Naurois, M. 2009, Contribution to the 31st ICRC, Lodz, Poland
Tetarenko, A. J., Casella, P., Miller-Jones, J. C. A., et al. 2019, MNRAS, 484, 2987
Torres, D. F., & Reimer, A. 2011, A&A, 528, L2
Zanin, R., Fernández-Barral, A., de Oña Wilhelmi, E., et al. 2016, A&A, 596, A55
Zdziarski, A. A., & Egron, E. 2022, ApJ, 935, L4
Zhang, J., Xu, B., & Lu, J. 2014, ApJ, 788, 143
Zhang, J.-F., Li, Z.-R., Xiang, F.-Y., & Lu, J.-F. 2017, MNRAS, 473, 3211

## Appendix A: Normalization constants

### A.1. Proton source function

The normalization constant for the relativistic proton source function depends on the lower and upper limit of their energy, as follows:

$$Q_0 = \frac{8 q_r L_k}{z_0 r_0^2 ln(E_p^{max}/E_p^{min})}, \tag{A.1}$$

where $r_0$ is the jet radius that corresponds to $z_0$. In addition, $E_p^{min} = 1.2\,GeV$ is the minimum proton energy that is sufficient and necessary for the Fermi mechanism to occur.

### A.2. Corona photon density

The normalization constant for the corona's photon density is given by

$$K_0 = \frac{4 L_c}{4\pi c \left(\epsilon_{max}^4 - \epsilon_{min}^4\right) R_c^2}, \tag{A.2}$$

where $L_c$ is the total corona luminosity (see Table 1) and $(\epsilon_{min} - \epsilon_{max}) \approx 10\,keV$-$100\,keV$ is the hard X-ray energy range.

## Appendix B: Cross-sections

### B.1. p-p interaction

The inelastic cross-section for the p-p scattering is given by (Kelner et al. 2006)

$$\sigma_{pp}^{inel}(E_p) = \left(0.25L^2 + 1.88L + 34.3\right) \times \left[1 - \left(\frac{E_{th}}{E_p}\right)^4\right]^2 \times 10^{-27}\,cm^2, \tag{B.1}$$

where $L = ln(E_p/1000)$, with $E_p$ in GeV and $E_{th} = 1.2\,GeV$, which is the threshold for producing a single neutral pion.

**Table B.1.** Constants that are used in the calculations.

| Constant | Value | Units |
|---|---|---|
| $c$ | $2.998 \times 10^{10}$ | $cms^{-1}$ |
| $M_\odot$ | $1.989 \times 10^{33}$ | $g$ |
| $G$ | $6.674 \times 10^{-8}$ | $cm^3 g^{-1} s^{-2}$ |
| $e$ | $4.803 \times 10^{-10}$ | $statC\ (cm^{3/2} g^{1/2} s^{-1})$ |
| $h$ | $6.626 \times 10^{-27}$ | $ergs$ |
| $k_B$ | $1.381 \times 10^{-16}$ | $ergK^{-1}$ |
| $\sigma_T$ | $6.652 \times 10^{-25}$ | $cm^2$ |
| $\sigma_{SB}$ | $5.670 \times 10^{-5}$ | $ergs^{-1} cm^{-2} K^{-4}$ |

### B.2. $\gamma$-$\gamma$ interaction

The cross-section of the interaction between two photons resulting in pair production is given below (Gould & Schréder 1967):

$$\sigma_{\gamma\gamma}(E_\gamma, \epsilon, \theta_0) = \frac{\pi e^4}{2m^2c^4}\left(1 - \beta^2\right) \times \left[\left(3 - \beta^4\right) ln\left(\frac{1+\beta}{1-\beta}\right) - 2\beta\left(2 - \beta^2\right)\right], \tag{B.2}$$

where $\theta_0$ is the angle between the two photons and $\epsilon$ the energy of the less energetic photon. In the above cross-section, $\beta$ is given by

$$\beta = \sqrt{1 - \frac{1}{s}}, \tag{B.3}$$

where

$$s = \frac{\epsilon E_\gamma (1 - \cos\theta_0)}{2m^2c^4}. \tag{B.4}$$

For annihilation to happen, it must be $s > 1$.